Volume Integral Equation Methods for Axisymmetric Problems With Conductive and Magnetic Media

R Torchio, D Voltolina, F Moro, P Alotto, P Bettini, Gérard Meunier, J-M Guichon, Olivier Chadebec

Volume Integral Equation Methods for Axisymmetric Problems with Conductive and Magnetic Media

R. Torchio[1,2], D. Voltolina[1], F. Moro[1], P. Alotto[1], P. Bettini[1], G. Meunier[2], J.-M. Guichon[2], and O. Chadebec[2]
[1]Dipartimento di Ingegneria Industriale, Università degli Studi di Padova, 35131 Padova, Italy
[2]Univ. Grenoble Alpes, CNRS, Grenoble INP, G2Elab, 28000 Grenoble, France

Two new different integral equation methods for the study of axisymmetric harmonic electromagnetic problems are presented. Both the proposed formulations allow for the modeling of conductive and magnetic media and inhomogeneous media can be considered as well. Thanks to the use of low–rank approximation techniques a drastic reduction of the required memory and computational cost is achieved with a truly negligible loss of accuracy. The numerical features of the two proposed integral methods are widely discussed and compared. Moreover, most of the considerations hold for the case of 3–D integral methods. Sample codes of the two formulations are made available at https://github.com/UniPD-DII-ETCOMP/DenseMatrixMarket.

***Index Terms*—Axisymmetric, magnetic media, low–rank approximation, hierarchical matrix, induction heating.**

I. Introduction

When complex electromagnetic (EM) devices are embedded in a large air domain or when small air gaps are present integral equations (IE) formulations can be more convenient than differential ones [1]. Several electromagnetic applications, such as induction hardening [2], induction cooking [3], EM levitation for melting devices [4], high temperature superconducting bearings [5], [6], and thermonuclear fusion devices [7], allow for an axisymmetric solution of the EM problem. Therefore, when the axisymmetric assumption actually holds, this property can be exploited to reduce the computational cost required by the numerical simulations of 3–D EM devices. Furthermore, on the contrary of differential methods, when devices with moving source coils are studied (e.g. in induction heating hardening processes) integral formulations do not require the re–mesh of the domains, which generally requires a non–negligible time, and a small quantity of mutual coefficients must be re–computed instead.

In this paper, two different IE methods for the study of axisymmetric EM problems involving conductive and magnetic media are presented. The first relies on the *amperian* interpretation of the magnetization phenomena while the second relies on the *coulombian* interpretation [8]. These two methods are derived from the 3–D Partial Element Equivalent Circuit (PEEC) formulations proposed in [9] and [10], respectively, and compared in [11]. Such as 3–D formulations, the two proposed methods show different numerical features which are compared and discussed. To the best of the author's knowledge, no axisymmetric integral formulation has been proposed in literature for the study of *both* conductive and magnetic media.

The case of dielectric media is not considered here. Indeed, when the axisymmetric assumption holds, the polarization currents are forced to be divergence free. Thus, the main effect of dielectric media (i.e. the enhancement of capacitive effects due to the bound electric charges) is not present. However, following [9] and [10], both the proposed methods can be easily extended to the case of dielectric media.

Like all the IE methods, the main drawback of the two proposed formulations is the generation of full matrices. However, thanks to the use of low–rank approximation techniques, the memory requirement and the computation time can be drastically reduced to a very small percentage of the cost required by the full matrix problem. Indeed, thanks to the smoothness of the axisymmetric kernel, a very low compression ratio can be obtained, e.g. less then 3% (lower than the ones usually attained in 3–D problems [12], [13]). Thus, the use of low–rank approximation techniques widely increases the applicability of the proposed formulations.

The rest of the paper is organized as follows. First, in section II, the *amperian* method is formulated and then discretized. Then, in section III, a different method based on the *coulombian* interpretation is proposed. In section IV, the numerical features of the two methods are discussed and compared. Most of the discussions still hold for the related 3–D methods proposed in [9] and [10]. Then, in section V, the case of a realistic induction cookware, presented in [14], is considered.

II. Amperian Method

The 3–D conductive and magnetic domains are defined as Ω_c and Ω_m, respectively. These domains can intersect and their union is defined as the active domain $\Omega_a = \Omega_c \cup \Omega_m$. These domains are obtained from the axial revolution of 2–D domains $\bar{\Omega}_c$, $\bar{\Omega}_m$, and $\bar{\Omega}_a$, i.e. $\Omega_c = \bar{\Omega}_c \times [0, 2\pi]$, $\Omega_m = \bar{\Omega}_m \times [0, 2\pi]$, and $\Omega_a = \bar{\Omega}_a \times [0, 2\pi]$. The boundaries of Ω_c and Ω_m are defined as $\Gamma_c = \partial\Omega_c$ and $\Gamma_m = \partial\Omega_m$, respectively, and analogously $\Gamma_c = \bar{\Gamma}_c \times [0, 2\pi]$, $\Gamma_m = \bar{\Gamma}_m \times [0, 2\pi]$, where $\bar{\Gamma}_c = \partial\bar{\Omega}_c$ and $\bar{\Gamma}_m = \partial\bar{\Omega}_m$.

A. Formulation

As in [9], the vector potential $\mathbf{A}$ and the scalar electric potential φ_e are introduced together with

$$\mathbf{E}(\mathbf{r}) = -i\omega\mathbf{A}(\mathbf{r}) - \nabla\varphi_e(\mathbf{r}) + \mathbf{E}_{ext}(\mathbf{r}), \quad (1)$$

$$\mathbf{B}(\mathbf{r}) = \nabla \times \mathbf{A}(\mathbf{r}) + \mathbf{B}_{ext}(\mathbf{r}), \quad (2)$$

Manuscript received December 1, 2012; revised August 26, 2015. Corresponding author: M. Shell (email: http://www.michaelshell.org/contact.html).

where $\mathbf{E}$ is the electric field, $\mathbf{B}$ is the magnetic flux density field, $\mathbf{r}$ is the field point, i is the imaginary unit, and ω is the angular frequency. $\mathbf{E}_{ext}$ and $\mathbf{B}_{ext}$ are the external electric and magnetic flux density fields. Equations (1) and (2) are complemented by the following constitutive relationships:

$$\mathbf{E}(\mathbf{r}) = \rho_c(\mathbf{r})\mathbf{J}_c(\mathbf{r}), \ \mathbf{r} \in \Omega_c \tag{3}$$

$$\mathbf{B}(\mathbf{r}) = \alpha_m(\mathbf{r})\mathbf{M}(\mathbf{r}), \ \mathbf{r} \in \Omega_m \tag{4}$$

where $\mathbf{J}_c$ is the conduction current density, $\mathbf{M}$ is the magnetization, ρ_c is the electric resistivity and

$$\alpha_m(\mathbf{r}) = \mu_0\mu_r(\mathbf{r})(\mu_r(\mathbf{r}) - 1)^{-1}, \tag{5}$$

in which μ_0 is the permeability of vacuum and μ_r is the relative permeability.

When the axisymmetric assumption holds, the EM quantities can be written in terms of cylindrical coordinates $(\vec{r}, \vec{\phi}, \vec{z})$. The vector EM quantities only exhibits some (cylindrical) coordinates, i.e.

$$\begin{aligned} \mathbf{J}_c = J_{c_\phi}\vec{\phi}, \quad \mathbf{J}_a = J_{a_\phi}\vec{\phi}, \quad \mathbf{K}_a = K_{a_\phi}\vec{\phi}, \quad \mathbf{E} = E_\phi\vec{\phi}, \\ \mathbf{A} = A_\phi\vec{\phi}, \quad \mathbf{B} = B_r\vec{r} + B_z\vec{z}, \quad \mathbf{M} = M_r\vec{r} + M_z\vec{z}. \end{aligned} \tag{6}$$

where $\mathbf{J}_a = \nabla \times \mathbf{M}$ and $\mathbf{K}_a = \mathbf{M} \times \mathbf{n}$ are the volume and surface *amperian* currents (in which $\mathbf{n}$ is the outgoing unit normal of Γ_m). It is worth noting that the axisymmetric condition (6) assumes the magneto–quasistatic hypothesis, i.e. capacitive and time–delay effects are neglected.

By imposing the Lorenz gauge condition $\nabla \cdot \mathbf{A} = -i\omega\varepsilon_0\mu_0\varphi_e$, where ε_0 is the permittivity of vacuum, an integral expression of $\mathbf{A}$ can be derived by combining (1) and (2) with the axisymmetric Maxwell's equations [20], i.e.

$$\begin{aligned} A_\phi(\mathbf{r}) = \mu_0 \Big[\int_{\bar{\Omega}_c} g(\mathbf{r}, \mathbf{r}') J_{c_\phi}(\mathbf{r}') d\bar{\Omega} \\ + \int_{\bar{\Omega}_m} g(\mathbf{r}, \mathbf{r}') J_{a_\phi}(\mathbf{r}') d\bar{\Omega} + \int_{\bar{\Gamma}_m} g(\mathbf{r}, \mathbf{r}') K_{a_\phi}(\mathbf{r}') d\bar{\Gamma} \Big], \end{aligned} \tag{7}$$

where $\mathbf{r}'$ is the integration point and $g(\mathbf{r}, \mathbf{r}')$ is the axisymmetric Green's function [16]. The field and the integration points can be written in cylindrical coordinates, i.e. $\mathbf{r} = (r, z, \phi)$ and $\mathbf{r}' = (r', \phi', z')$. The axisymmetric Green's function (which is the solution of the Poisson equation for a ring carrying a uniform current [19]) is defined as

$$g(\mathbf{r}, \mathbf{r}') = \frac{4r'}{K} \frac{(2 - k^2)\mathcal{K}(k^2) - 2\mathcal{E}(k^2)}{4\pi k^2}, \tag{8}$$

where

$$K = \sqrt{(r' + r)^2 + (z' - z)^2}, \qquad k^2 = 4r'rK^{-2}, \tag{9}$$

and $\mathcal{K}$ and $\mathcal{E}$ are the *elliptic integrals* of the first and second kind, respectively (defined with the same convention of [20]).

The axisymmetry assumption (6) enforces the solenoidality of $\mathbf{J}_c$. Thus, since the volume and surface electric charges vanish (which are the sources of φ_e), the scalar electric potential is null, i.e. $\varphi_e(\mathbf{r}) = 0$.

Finally, under the axisymmetry assumption, combining (1) and (2) with (3) and (4), respectively, the final continuum equations for an axisymmetric EM problem are

$$\rho_c(\mathbf{r})\mathbf{J}_c(\mathbf{r}) = -i\omega\mathbf{A}(\mathbf{r}) + \mathbf{E}_{ext}(\mathbf{r}), \ \mathbf{r} \in \Omega_c, \tag{10}$$

$$\alpha_m(\mathbf{r})\mathbf{M}(\mathbf{r}) = \nabla \times \mathbf{A}(\mathbf{r}) + \mathbf{B}_{ext}(\mathbf{r}), \ \mathbf{r} \in \Omega_m, \tag{11}$$

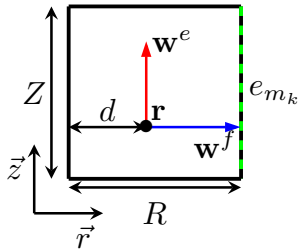

Figure 1. Axial–symmetric vector edge (red) and face (blue) shape functions related to edge e_{m_k}. An equivalent representation holds for edges along the r direction.

where $\mathbf{A}$ is given by the integral expression (7).

B. Discretization

The 2–D domains $\bar{\Omega}_c$ and $\bar{\Omega}_m$ in the (r, z) plane (i.e. $\phi = 0$) are discretized into two quadrilateral grids defined as: $\mathcal{G}_{\bar{\Omega}_c}$ for $\bar{\Omega}_c$, and $\mathcal{G}_{\bar{\Omega}_m}$ for $\bar{\Omega}_m$. $\mathcal{G}_{\bar{\Omega}_c}$ consists of n_c nodes, e_c edges, and f_c faces. Similarly, $\mathcal{G}_{\bar{\Omega}_m}$ consists of n_m nodes, e_m edges, and f_m faces. The two grids overlap when a conductive magnetic media is considered.

The conduction current density vector is then expanded as

$$\mathbf{J}_c(\mathbf{r}) = \sum_k^{f_c} \mathbf{w}_k^\phi(\mathbf{r}) j_{c_k}, \tag{12}$$

where j_{c_k} is the flux of $\mathbf{J}_c$ through the kth quadrilateral face of $\mathcal{G}_{\bar{\Omega}_c}$ and $\mathbf{w}_k^\phi$ is the *azimuthal* vector shape function related to f_{c_k}. The corresponding arrays of DoFs $\mathbf{j}_c = (j_{c_k})$ is then introduced. The shape function $\mathbf{w}_k^\phi$ is defined as

$$\mathbf{w}_k^\phi(\mathbf{r}) = A_k^{-1}\vec{\phi}, \ \mathbf{r} \in f_k, \tag{13}$$

where A_k is the area of f_{c_k}.

The magnetization is instead discretized as

$$\mathbf{M}(\mathbf{r}) = \sum_k^{e_m} \mathbf{w}_k^e(\mathbf{r}) m_k, \tag{14}$$

where $m_k = \int_{e_m} \mathbf{M} \cdot d\mathbf{l}$ is the line integral of $\mathbf{M}$ along the kth edge of the mesh e_{m_k} and $\mathbf{w}_k^e$ is the axisymmetric edge shape function related to e_{m_k}. The array of DoFs $\mathbf{m} = (m_k)$ is introduced. The vector shape function $\mathbf{w}_k^e$ is obtained as the axial revolution of the (traditional) edge vector shape function. With respect to Fig. 1, $\mathbf{w}_k^e$ is given by

$$\mathbf{w}_k^e(\mathbf{r}) = \mathbf{w}_k^e(r, z, \phi) = \begin{cases} \frac{d}{ZR}\vec{e}_k, & \mathbf{r} \in \Delta_k \\ 0, & elsewhere \end{cases}, \tag{15}$$

where $\vec{e}_k$ is the unit vector in the direction of the e_{m_k} and Δ_k is the support of $\mathbf{w}_k^e$, i.e. the quadrilateral faces having e_{m_k}.

It is useful to introduce also the expansions of $\mathbf{J}_a$ and $\mathbf{K}_a$. $\mathbf{J}_a$ is expanded similarly to (12) and the vector array $\mathbf{j}_a = (j_{a_k})$ is introduced where j_{a_k} is the flux of $\mathbf{J}_a$ through the kth quadrilateral face of $\mathcal{G}_{\bar{\Omega}_m}$. Analogously, the surface amperian currents $\mathbf{K}_a$ are expanded as

$$\mathbf{K}_a(\mathbf{r}) = \sum_k^{e_m^b} \mathbf{w}_k^{\phi s}(\mathbf{r}) k_{a_k}, \tag{16}$$

where k_{a_k} is the flux of $\mathbf{K}_a$ through the kth *boundary* edge $e_{m_k}^b$ of $\mathcal{G}_{\bar{\Omega}_m}$. Then, the array of DoFs $\mathbf{k}_a = (k_{a_k})$ is

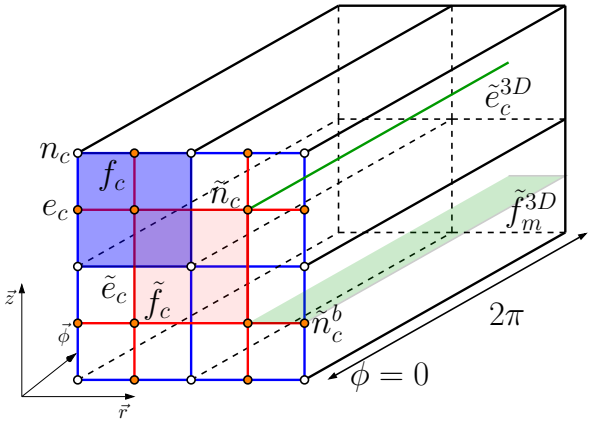

Figure 2. Primal and dual geometric entities for the conductive grid. Rectified axisymmetric geometry

introduced. $\mathbf{w}_k^{\phi s}$ is the azimuthal vector shape function related to $e^b_{m_k}$ and defined as

$$\mathbf{w}_k^{\phi s}(\mathbf{r}) = L_k^{-1}\vec{\phi},\ \mathbf{r} \in e_k^b, \tag{17}$$

where L_k is the length of $e^b_{m_k}$.

The dual grids $\tilde{\mathcal{G}}_{\bar{\Omega}_c}$ and $\tilde{\mathcal{G}}_{\bar{\Omega}_m}$ obtained from the barycentric subdivision of $\mathcal{G}_{\bar{\Omega}_c}$ and $\mathcal{G}_{\bar{\Omega}_m}$ are now defined. These grids consist of *dual* geometric entities: $\tilde{\mathcal{G}}_{\bar{\Omega}_c}$ consists of *dual* $\tilde{n}_c$ nodes, $\tilde{e}_c$ edges, and $\tilde{f}_c$ faces, while $\tilde{\mathcal{G}}_{\bar{\Omega}_m}$ consists of *dual* $\tilde{n}_m$ nodes, $\tilde{e}_m$ edges, and $\tilde{f}_m$ faces. The geometric entities of $\mathcal{G}_{\bar{\Omega}_c}$ and the dual grid $\tilde{\mathcal{G}}_{\bar{\Omega}_c}$ are exemplified in Fig. 4 for a rectified geometry. Thus, the following arrays of DoFs associated to the geometric entities of $\tilde{\mathcal{G}}_{\bar{\Omega}_c}$ can be defined

- $\mathbf{e} = (e_k)$ on dual nodes $\tilde{n}_c$, where

$$e_k = 2\pi r_{\tilde{n}_c} E_\phi(\mathbf{r}_{\tilde{n}_c}), \tag{18}$$

- $\mathbf{a}^c = (a_k^c)$ on dual nodes $\tilde{n}_c$, where

$$a_k^c = 2\pi r_{\tilde{n}_c} A_\phi(\mathbf{r}_{\tilde{n}_c}), \tag{19}$$

in which $\mathbf{r}_{\tilde{n}_c} = (r_{\tilde{n}_c}, \phi_{\tilde{n}_c}, z_{\tilde{n}_c})$ is the position of the kth dual node $\tilde{n}_{c_k}$. The array of DoFs $\mathbf{e}_0$ related to $\mathbf{E}_{ext}$ is defined likewise $\mathbf{e}$. It is worth noting that, due to the axisymmetric assumption, the dual nodes $\tilde{n}_c$ are in a one–to–one relationship with the 3–D (dual) edges $\tilde{e}_c^{3D}$ obtained as the axial revolution of $\tilde{n}_c$, as represented in Fig. 4. Indeed, (18) and (19) are equal to the line integrals of $\mathbf{E}$ and $\mathbf{A}$ along the kth 3–D edge $\tilde{e}^{3D}_{c_k}$.

Other arrays of DoFs related to $\mathbf{B}$ and $\mathbf{A}$ can also be introduced for the dual magnetic grid $\tilde{\mathcal{G}}_{\bar{\Omega}_m}$:

- $\mathbf{a}^m = (a_k^m)$ on dual nodes $\tilde{n}_m$, where

$$a_k^m = 2\pi r_{\tilde{n}_m} A_\phi(\mathbf{r}_{\tilde{n}_m}); \tag{20}$$

  $\mathbf{a}^m$ can be subdivided into $\mathbf{a}^m = [\mathbf{a}^{mv}, \mathbf{a}^{ms}]$, where $\mathbf{a}^{mv}$ is related to the *internal* dual nodes and $\mathbf{a}^{ms}$ is related to the *boundary* dual nodes;
- $\mathbf{b} = (b_k)$ on dual edges $\tilde{e}_m$, where

$$b_k = \int_{e_{m_k}} 2\pi r(\vec{\phi} \times \mathbf{B}) \cdot d\mathbf{l}, \tag{21}$$

  i.e. b_k is the flux of $\mathbf{B}$ trough the 3–D (dual) face $\tilde{f}^{3D}_{m_k}$ obtained as the axial revolution of $\tilde{e}_{m_k}$ (see Fig. 4).

The array of DoFs $\mathbf{b}_0$ related to $\mathbf{B}_{ext}$ is defined likewise $\mathbf{b}$. Expansions (12), (14) and (16) can now be inserted in (10) and (11). Then, the resulting equations are tested following the Galerkin scheme, i.e. (10) is tested with $\mathbf{w}_k^\phi$, for $k = 1, \cdots, f_c$, and (11) is tested with $\mathbf{w}_k^e$, for for $k = 1, \cdots, e_m$. Thus, equations which represent the discrete form of (1) and (2) are

$$\mathbf{e} + i\omega\mathbf{a}^c = \mathbf{e}_0, \tag{22}$$

$$\mathbf{b} + \tilde{\mathbf{G}}_{\bar{\Omega}_m}\mathbf{a}^m = \mathbf{b}_0, \tag{23}$$

where $\tilde{\mathbf{G}}_{\bar{\Omega}_m}$ is the *dual edge to dual node* (dual) incidence matrix of dimension $(\tilde{e}_m \times \tilde{n}_m)$.

The discrete forms of (3) and (4) result in

$$\mathbf{e} = \mathbf{R}_c\mathbf{j}_c, \qquad \mathbf{b} = \mathbf{F}\mathbf{m}, \tag{24}$$

where $\mathbf{R}$ and $\mathbf{F}$ are sparse constitutive matrices:

$$R_{c,kh} = \int_{\bar{\Omega}_c} 2\pi r \mathbf{w}_k^\phi(\mathbf{r}) \cdot \mathbf{w}_h^\phi(\mathbf{r})\rho_c(\mathbf{r})d\bar{\Omega}, \tag{25}$$

$$F_{kh} = \int_{\bar{\Omega}_m} 2\pi r \mathbf{w}_k^e(\mathbf{r}) \cdot \mathbf{w}_h^e(\mathbf{r})\alpha_m(\mathbf{r})d\bar{\Omega}. \tag{26}$$

The arrays $\mathbf{a}^c$ and $\mathbf{a}^m = [\mathbf{a}^{mv}, \mathbf{a}^{ms}]$, are instead obtained as

$$\begin{aligned}
\mathbf{a}^c &= \mathbf{L}_c^c\mathbf{j}_c + \mathbf{L}_m^c\mathbf{j}_a + \mathbf{L}_{ms}^c\mathbf{k}_a,\\
\mathbf{a}^{mv} &= \mathbf{L}_c^m\mathbf{j}_c + \mathbf{L}_m^m\mathbf{j}_a + \mathbf{L}_{ms}^m\mathbf{k}_a,\\
\mathbf{a}^{ms} &= \mathbf{L}_c^{ms}\mathbf{j}_c + \mathbf{L}_m^{ms}\mathbf{j}_a + \mathbf{L}_{ms}^{ms}\mathbf{k}_a,
\end{aligned} \tag{27}$$

in which the *volume*, *surface*, and *volume–surface* inductance matrices are defined as

$$\begin{aligned}
L^\alpha_{\beta_{ku}} &= \mu_0 \int_{\bar{\Omega}_\beta} 2\pi r \mathbf{w}_u^\phi(\mathbf{r}) \cdot \int_{\bar{\Omega}_\alpha} \mathbf{w}_k^\phi(\mathbf{r}')g(\mathbf{r},\mathbf{r}')d\bar{\Omega}'d\bar{\Omega},\\
L^{ms}_{\alpha_{ku}} &= \mu_0 \int_{\bar{\Omega}_\alpha} 2\pi r \mathbf{w}_u^\phi(\mathbf{r}) \cdot \int_{\bar{\Gamma}_m} \mathbf{w}_k^{\phi s}(\mathbf{r}')g(\mathbf{r},\mathbf{r}')d\bar{\Gamma}'d\bar{\Omega},\\
L^{ms}_{ms_{uk}} &= \mu_0 \int_{\bar{\Gamma}_m} 2\pi r \mathbf{w}_u^{\phi s}(\mathbf{r}) \cdot \int_{\bar{\Gamma}_m} \mathbf{w}_k^{\phi s}(\mathbf{r}')g(\mathbf{r},\mathbf{r}')d\bar{\Gamma}'d\bar{\Gamma},
\end{aligned}$$

where $\alpha = c, m$, $\beta = c, m$, $L^\alpha_{\beta_{ku}} = L^\beta_{\alpha_{uk}}$, and $L^{ms}_{\alpha_{ku}} = L^\alpha_{ms_{uk}}$.

Moreover, $\mathbf{j}_a$, $\mathbf{k}_a$, and $\mathbf{m}$ satisfy:

$$\mathbf{j}_a = \mathbf{C}_{\bar{\Omega}_m}\mathbf{m}, \qquad \mathbf{k}_a = \mathbf{C}_{\bar{\Omega}_m}\mathbf{m}, \qquad \begin{bmatrix}\mathbf{j}_a\\ \mathbf{k}_a\end{bmatrix} = \mathbf{C}^a_{\bar{\Omega}_m}\mathbf{m}, \tag{28}$$

where $\mathbf{C}_{\bar{\Omega}_m}$ is the $(f_m \times e_m)$ *face to edge* incidence matrix, $\mathbf{C}_{\bar{\Gamma}_m}$ is the $(e^b_m \times e_m)$ selection matrix which selects the boundary edges e^b_m of $\mathcal{G}_{\bar{\Omega}_m}$, and $\mathbf{C}^a_{\bar{\Omega}_m} = \begin{bmatrix}\mathbf{C}_{\bar{\Omega}_m}\\ \mathbf{C}_{\bar{\Gamma}_m}\end{bmatrix} = \tilde{\mathbf{G}}^T_{\bar{\Omega}_m}$.

Finally, the discrete EM problem can be represented as the following algebraic system of equations

$$\begin{bmatrix} \mathbf{R}_c + i\omega\mathbf{L}_c^c & i\omega[\mathbf{L}_m^c, \mathbf{L}_{ms}^c]\mathbf{C}^a_{\bar{\Omega}_m}\\ -\tilde{\mathbf{G}}_{\bar{\Omega}_m}\begin{bmatrix}\mathbf{L}_c^m\\ \mathbf{L}_c^{ms}\end{bmatrix} & \mathbf{F} - \tilde{\mathbf{G}}_{\bar{\Omega}_m}\begin{bmatrix}\mathbf{L}_m^m & \mathbf{L}_{ms}^m\\ \mathbf{L}_m^{ms} & \mathbf{L}_{ms}^{ms}\end{bmatrix}\mathbf{C}^a_{\bar{\Omega}_m}\end{bmatrix}\begin{bmatrix}\mathbf{j}_c\\ \mathbf{m}\end{bmatrix} = \begin{bmatrix}\mathbf{e}_0\\ \mathbf{b}_0\end{bmatrix}, \tag{29}$$

which can be symmetrized by multiplying the second row by $-i\omega$. System (29) naturally enforce the EM properties of the magnetization, but not in a numerically strong sense. For instance, in steady state condition and for homogeneous non–conductive magnetic media, only the surface amperian currents exist while the volume amperian currents are zero ($\nabla \times \mathbf{M} = \mathbf{J}_a \approx 0$). This condition is not strongly enforced by (29) and a distribution of $\mathbf{J}_a$ close to the boundary is obtained

also when a zero frequency problem is solved. Anyhow, this usually does not particularly affect the global quality of the solution but it can be an issue when high accuracy is required. However, this condition can be enforced by imposing:

$$\mathbf{m} = \mathbf{G}_{\bar{\Omega}_m} \boldsymbol{\psi}_m, \tag{30}$$

where $\mathbf{G}_{\bar{\Omega}_m}$ is the *edge to node* $(e_m \times n_m)$ incidence matrix and $\boldsymbol{\psi}_m$ is the array of DoFs related to a *discrete scalar magnetic potential* associated to the primal nodes n_m of $\mathcal{G}_{\bar{\Omega}_m}$ (one node for each magnetic sub–domain must be removed and considered as reference). Thus, when $\nabla \times \mathbf{M}$ holds, (30) can be applied to (29) and the second row of (29) can be projected into a new set of equations by using $\mathbf{G}^T_{\bar{\Omega}_m}$ (without one row for each magnetic sub–domain). The resulting system has a reduced dimension and, since $\mathbf{j}_a = 0$, the evaluation of $\mathbf{L}^m_c$, $\mathbf{L}^c_m$, and $\mathbf{L}^m_m$ is not needed anymore.

III. Coulombian Method

In the following an alternative method for the study of axisymmetric EM problems is proposed. In section II, the magnetization phenomena have been considered following the amperian interpretation. Here, instead, the *magnetic currents and charges* are introduced and different electric and magnetic potentials are adopted.

A. Formulation

Equations (1) and (4) can be replaced by the following

$$\mathbf{E}(\mathbf{r}) = -i\omega\mathbf{A}_e(\mathbf{r}) - \nabla\varphi_e(\mathbf{r}) - \varepsilon_0^{-1}\nabla \times \mathbf{A}_m(\mathbf{r}) + \mathbf{E}_{ext}(\mathbf{r}), \tag{31}$$

$$\mathbf{H}(\mathbf{r}) = -i\omega\mathbf{A}_m(\mathbf{r}) - \nabla\varphi_m(\mathbf{r}) + \mu_0^{-1}\nabla \times \mathbf{A}_e(\mathbf{r}) + \mathbf{H}_{ext}(\mathbf{r}), \tag{32}$$

where $\mathbf{A}_e$ and $\mathbf{A}_m$ are the electric and magnetic vector potentials [10], φ_m is the scalar magnetic potential, $\mathbf{H}(\mathbf{r})$ is the magnetic field, and $\mathbf{H}_{ext}(\mathbf{r})$ is the external magnetic field.

The vector potentials $\mathbf{A}_e$ and $\mathbf{A}_m$ are related to $\mathbf{A}$ by

$$\mathbf{A} = \mathbf{A}_e + (i\omega)^{-1}\nabla \times \mathbf{A}_m, \tag{33}$$

and they are defined as in [10] together with φ_m. The Lorenz gauge conditions are also imposed: $\nabla \cdot \mathbf{A}_e = -i\omega\varepsilon_0\mu_0\varphi_e$ and $\nabla \cdot \mathbf{A}_m = -i\omega\varepsilon_0\mu_0\varphi_m$.

Relations (6) still hold and they are complemented with

$$\begin{aligned} \mathbf{A}_e &= A_{e_\phi}\vec{\phi}, \qquad & \mathbf{H} &= H_r\vec{r} + H_z\vec{z}, \\ \mathbf{J}_m &= J_{m_r}\vec{r} + J_{m_r}\vec{z}, \qquad & \mathbf{A}_m &= A_{m_r}\vec{r} + A_{m_r}\vec{z}. \end{aligned} \tag{34}$$

where $\mathbf{J}_m = i\omega\mu_0\mathbf{M}$ is the magnetic current density.

As noticed in section II, when the axisymmetric assumption holds, $\mathbf{J}_c$ is divergence free and $\varphi_e(\mathbf{r}) = 0$.

The integral expression of $\mathbf{A}_e$ can be formulated in cylindrical coordinates as shown in [20]:

$$A_{e_\phi}(\mathbf{r}) = \mu_0 \int_{\bar{\Omega}_c} g(\mathbf{r}, \mathbf{r}') J_{c_\phi}(\mathbf{r}') d\Omega, \tag{35}$$

with the same definition given for (7).

The definition of φ_m can be also derived from [20]:

$$\varphi_m(\mathbf{r}) = \int_{\bar{\Omega}_m} \frac{\bar{g}(\mathbf{r}, \mathbf{r}')}{\mu_0} \varrho_m(\mathbf{r}') d\bar{\Omega} + \int_{\bar{\Gamma}_m} \frac{\bar{g}(\mathbf{r}, \mathbf{r}')}{\mu_0} \varsigma_m(\mathbf{r}') d\bar{\Gamma}, \tag{36}$$

where, ϱ_m and ς_m are the volume and surface bound magnetic charges related to $\mathbf{J}_m$ by means of the continuity relations:

$$\nabla' \cdot \mathbf{J}_m(\mathbf{r}') = -i\omega\varrho_m(\mathbf{r}'), \qquad \mathbf{J}_m(\mathbf{r}') \cdot \mathbf{n} = -i\omega\varsigma_m(\mathbf{r}'). \tag{37}$$

In (36), $\bar{g}$ is the axisymmetric Green's function of the scalar potential. The axisymmetric Green's function $\bar{g}$ is the solution of the Poisson equation for a uniformly charged ring [17], [18], that is

$$\bar{g}(\mathbf{r}, \mathbf{r}') = \frac{4r'}{4\pi K}\mathcal{K}(k^2), \tag{38}$$

where the quantities are defined as in (8).

The axisymmetric integral expression of $\mathbf{A}_m$ can be extrapolated from the one of the scalar magnetic potential, i.e.

$$A_{m_\alpha}(\mathbf{r}) = \varepsilon_0 \int_{\bar{\Omega}_m} \bar{g}(\mathbf{r}, \mathbf{r}') J_{m_\alpha}(\mathbf{r}') d\Gamma, \tag{39}$$

where $\alpha = r, z$. Equations (31) and (32) are complemented by (3) and the following constitutive equation:

$$\mathbf{H}(\mathbf{r}) = \rho_m(\mathbf{r})\mathbf{J}_m(\mathbf{r}), \ \mathbf{r} \in \Omega_m, \tag{40}$$

where $\rho_m = (i\omega\mu_0(\mu_r - 1))^{-1}$ is the magnetic resistivity.

Finally, combining (31) with (3), and (32) with (40), the following final continuum equations for an EM axisymmetric problem are obtained

$$\begin{aligned} \rho_c(\mathbf{r})\mathbf{J}_c(\mathbf{r}) = &- i\omega\mathbf{A}_e(\mathbf{r}, \mathbf{J}_c(\mathbf{r}')) - \varepsilon_0^{-1}\nabla \times \mathbf{A}_m(\mathbf{r}, \mathbf{J}_m(\mathbf{r}')) \\ &+ \mathbf{E}_{ext}(\mathbf{r}), \ \mathbf{r} \in \Omega_c, \end{aligned} \tag{41}$$

$$\begin{aligned} \rho_m(\mathbf{r})\mathbf{J}_m(\mathbf{r}) = &- i\omega\mathbf{A}_m(\mathbf{r}, \mathbf{J}_m(\mathbf{r}')) - \nabla\varphi_m(\mathbf{r}, \mathbf{J}_m(\mathbf{r}')) \\ &+ \mu_0^{-1}\nabla \times \mathbf{A}_e(\mathbf{r}, \mathbf{J}_c(\mathbf{r}')) \\ &+ \mathbf{H}_{ext}(\mathbf{r}), \ \mathbf{r} \in \Omega_m, \end{aligned} \tag{42}$$

where $\mathbf{A}_e$, φ_m, and $\mathbf{A}_m$ are given by (35), (36), and (39), respectively.

B. Discretization

Conductive and magnetic domains are represented by means of 2–D domains $\bar{\Omega}_c$ and $\bar{\Omega}_m$ in the (r, z) plane (i.e. $\phi = 0$) as in section II. Again, the two quadrilateral grids $\mathcal{G}_{\bar{\Omega}_c}$ and $\mathcal{G}_{\bar{\Omega}_m}$ are introduced with the same definitions given above. Moreover, the dual grids $\tilde{\mathcal{G}}_{\bar{\Omega}_c}$ and $\tilde{\mathcal{G}}_{\bar{\Omega}_m}$ are also introduced and the conduction current $\mathbf{J}_c$ is expanded as in (12).

The only difference concerning conductive media between the two formulations is in the definition of the arrays of DoFs related to the vector potentials. In this formulation $\mathbf{A}$ is replaced by $\mathbf{A}_e$ and $\mathbf{A}_m$ and the corresponding arrays of DoFs are introduced:

- $\mathbf{a}^c_e = (a^c_{e,k})$ on dual nodes $\tilde{n}_c$, where

$$a^c_{e,k} = 2\pi r_{\tilde{n}_c} A_{e_\phi}(\mathbf{r}_{\tilde{n}_c}), \tag{43}$$

- $\mathbf{a}^c_m = (a^c_{m,k})$ on primal edges e_c, where

$$a^c_{m,k} = \int_{e_{m,k}} \mathbf{A}_m(\mathbf{r}) \cdot d\mathbf{l}. \tag{44}$$

The magnetic current density $\mathbf{J}_m$ is expanded as

$$\mathbf{J}_m(\mathbf{r}) = \sum_k^{e_m} \mathbf{w}^f_k(\mathbf{r}) j_{m,k}, \tag{45}$$

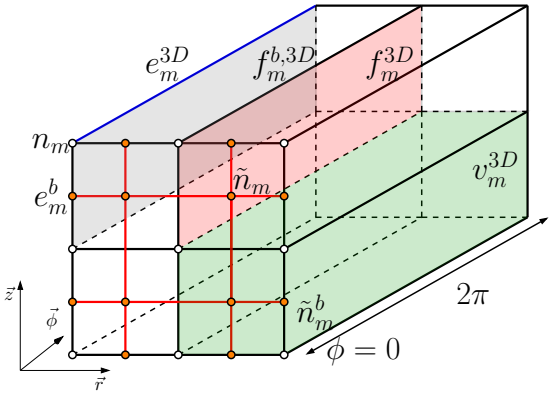

Figure 3. Primal and dual geometric entities of the magnetic grid for the coulombian formulation. Rectified axisymmetric geometry.

where

$$j_{m,k} = \int_{e_m} 2\pi r(\vec{\phi} \times \mathbf{J}_m(\mathbf{r})) \cdot d\mathbf{l},$$

is the flux of $\mathbf{J}_m$ through the kth 3–D face $f_{m_k}^{3D}$ represented in Fig. 3 and related to the kth dual edge e_{m_k} (i.e. $f_{m_k}^{3D}$ is the axial–revolution of e_{m_k}, as shown in Fig. 3). Thus, the corresponding array of DoFs $\mathbf{j}_m = (j_{m_k})$ is introduced. $\mathbf{w}_k^f$ is the (scaled) face vector shape function related to e_{m_k} and exemplified in Fig. 1. With respect to Fig. 1, $\mathbf{w}_k^f$ is given by

$$\mathbf{w}_k^f(\mathbf{r}) = \mathbf{w}_k^f(r,z,\phi) = \begin{cases} \frac{d}{A_k^{3D} R}(\vec{\phi} \times \vec{e}_k), & \mathbf{r} \in \Delta_k \\ 0, & elsewhere \end{cases}, \tag{46}$$

where A_k^{3D} is the area obtained from the axial revolution of e_{m_k} (i.e. the area of $f_{m_k}^{3D}$ and $A_k^{3D} = 2\pi Z$).

The expansion (45) combined with (37) induces an expansion for ϱ_m and ς_m. Thus, the continuity equations (37) in discrete form become

$$\begin{gathered} \mathbf{C}_{\bar{\Omega}_m}\mathbf{j}_m = -i\omega\mathbf{q}_m^v, \qquad \mathbf{C}_{\bar{\Gamma}_m}\mathbf{j}_m = -i\omega\mathbf{q}_m^s, \\ \mathbf{C}_{\bar{\Omega}_m}^a\mathbf{j}_m = -\,i\omega\left[\mathbf{q}_m^v, \mathbf{q}_m^s\right]^T, \end{gathered} \tag{47}$$

where $\mathbf{q}_m^v = (q_{m,k}^v)$, for $k = 1, \cdots, f_m$, and $\mathbf{q}_m^s = (q_{m,k}^s)$, for $k = 1, \cdots, e_m^b$, store the (net) volume and surface bound magnetic charges, respectively.

Additional arrays of DoFs living on the geometric entities of $\mathcal{G}_{\bar{\Omega}_m}$ and $\tilde{\mathcal{G}}_{\bar{\Omega}_m}$ can be introduced for $\mathbf{H}$, $\mathbf{A}_e$, $\mathbf{A}_m$, and φ_m:

- $\mathbf{h} = (h_k)$ on dual edges $\tilde{e}_m$, where

$$h_k = \int_{\tilde{e}_{m,k}} \mathbf{H}(\mathbf{r}) \cdot d\mathbf{l}, \tag{48}$$

- $\mathbf{a}_m^m = (a_{m,k}^m)$ on dual edges $\tilde{e}_m$, where

$$a_{m,k}^m = \int_{\tilde{e}_{m,k}} \mathbf{A}_m(\mathbf{r}) \cdot d\mathbf{l}, \tag{49}$$

- $\boldsymbol{\phi}_m = (\phi_{m,k})$ on dual nodes $\tilde{n}_m$, where

$$\phi_{m,k}^v = \varphi_m(\mathbf{r}_{\tilde{n}_m}), \tag{50}$$

  $\boldsymbol{\phi}_m$ can be subdivided into $\boldsymbol{\phi}_m = [\boldsymbol{\phi}_m^v, \boldsymbol{\phi}_m^s]$, where $\boldsymbol{\phi}_m^v$ is related to the *internal* dual nodes and $\boldsymbol{\phi}_m^s$ is related to the *boundary* dual nodes,

- $\mathbf{a}_e^m = (a_{e,k}^m)$ on nodes n_m, where

$$a_{e,k}^m = 2\pi r_{n_m} A_{e_\phi}(\mathbf{r}_{n_m}), \tag{51}$$

The array of DoFs $\mathbf{h}_0$ related to $\mathbf{H}_0$ is defined likewise $\mathbf{h}$.

Expansions (12) and (45) are now inserted in (41) and (42). Then, the resulting equations are tested following the Galerkin scheme, i.e. (41) is tested with $\mathbf{w}_k^\phi$, for $k = 1, \cdots, f_c$, and (42) is tested with $\mathbf{w}_k^f$, for for $k = 1, \cdots, e_m$. The following equations represent the discrete form of (31) and (32):

$$\mathbf{e} + i\omega\mathbf{a}_e^c + \mathbf{M}_{1/\varepsilon_0}\mathbf{C}_{\bar{\Omega}_c}\mathbf{a}_m^c = \mathbf{e}_0, \tag{52}$$

$$\mathbf{h} + i\omega\mathbf{a}_m^m + \tilde{\mathbf{G}}_{\bar{\Omega}_m}\boldsymbol{\phi}_m - \mathbf{M}_{1/\mu_0}\mathbf{G}_{\bar{\Omega}_m}\mathbf{a}_e^m = \mathbf{h}_0, \tag{53}$$

where $\mathbf{C}_{\bar{\Omega}_c}$ is the *face to edge* conductive incidence matrix of dimension $(f_c \times e_c)$, while $\mathbf{M}_{1/\varepsilon_0}$ and $\mathbf{M}_{1/\mu_0}$ are projection matrices defined as

$$M_{1/\varepsilon_0,kh} = \frac{1}{\varepsilon_0}\int_{\bar{\Omega}_c} 2\pi r\mathbf{w}_k^\phi(\mathbf{r}) \cdot \mathbf{w}_h^\phi(\mathbf{r}) d\bar{\Omega}, \tag{54}$$

$$M_{1/\mu_0,ku} = \frac{1}{\mu_0}\int_{\bar{\Omega}_m} 2\pi r\mathbf{w}_u^f(\mathbf{r}) \cdot \mathbf{w}_k^f(\mathbf{r}) d\bar{\Omega}. \tag{55}$$

The discrete form of (3) is again given by the first equation in (24). Instead, the one of (40) is given by

$$\mathbf{h} = \mathbf{R}_m\mathbf{j}_m, \tag{56}$$

where $\mathbf{R}_m$ is a sparse constitutive matrix:

$$R_{m_{ku}} = \int_{\bar{\Omega}_m} 2\pi r\mathbf{w}_u^f(\mathbf{r}) \cdot \mathbf{w}_k^f(\mathbf{r})\rho_m(\mathbf{r}) d\bar{\Omega}. \tag{57}$$

The others arrays $\mathbf{a}_e^c$, $\mathbf{a}_m^c$, $\mathbf{a}_m^m$, $\mathbf{a}_e^m$, and $\boldsymbol{\phi}_m$ are instead obtained as

$$\begin{gathered} \mathbf{a}_e^c = \mathbf{L}_c^c\mathbf{j}_c, \quad \mathbf{a}_m^m = \mathbf{L}_m^m\mathbf{j}_m, \quad \mathbf{a}_m^c = \mathbf{N}_m^c\mathbf{j}_m, \quad \mathbf{a}_e^m = \mathbf{N}_c^m\mathbf{j}_c, \\ [\boldsymbol{\phi}_m^v, \boldsymbol{\phi}_m^s] = \mathbf{P}_m\begin{bmatrix}\mathbf{q}_m^v \\ \mathbf{q}_m^s\end{bmatrix} = \begin{bmatrix}\mathbf{P}_m^{vv} & \mathbf{P}_m^{vs} \\ \mathbf{P}_m^{sv} & \mathbf{P}_m^{ss}\end{bmatrix}\begin{bmatrix}\mathbf{q}_m^v \\ \mathbf{q}_m^s\end{bmatrix}, \end{gathered} \tag{58}$$

in which

$$P_{m_{ku}}^{vv} = \frac{1}{A_k V_u^{3D}\mu_0}\int_{f_{m_k}}\int_{f_{m_u}} \bar{g}(\mathbf{r},\mathbf{r}') d\bar{\Omega}' d\bar{\Omega}, \tag{59}$$

where V_u^{3D} is the volume of the uth 3–D volume $v_{m_u}^{3D}$ (i.e. the axial revolution of f_{m_u}) and A_k is the area of f_{m_k};

$$P_{m_{ku}}^{sv} = \frac{1}{L_k V_u^{3D}\mu_0}\int_{e_{m_k}^b}\int_{f_{m_u}} \bar{g}(\mathbf{r},\mathbf{r}') d\bar{\Omega}' d\bar{\Gamma}, \tag{60}$$

where L_k is the length of the boundary edge $e_{m_k}^b$;

$$P_{m_{ku}}^{vs} = \frac{1}{A_k A_u^{3D}\mu_0}\int_{f_{m_k}}\int_{e_{m_u}^b} \bar{g}(\mathbf{r},\mathbf{r}') d\bar{\Gamma}' d\bar{\Omega}, \tag{61}$$

where A_u^{3D} is the area of the uth 3–D face $f_{m_u}^{b,3D}$ (i.e. the axial revolution of $e_{m,u}^b$);

$$P_{m_{ku}}^{ss} = \frac{1}{L_k A_u^{3D}\mu_0}\int_{e_{m,k}^b}\int_{e_{m,u}^b} \bar{g}(\mathbf{r},\mathbf{r}') d\bar{\Gamma}' d\bar{\Gamma}. \tag{62}$$

The magnetic inductance matrix $\mathbf{L}_m^m$ is instead given by

$$L_{m_{ku}}^m = \varepsilon_0\int_{\bar{\Omega}_m} 2\pi r\mathbf{w}_u^f(\mathbf{r}) \cdot \int_{\bar{\Omega}_m} \mathbf{w}_k^f(\mathbf{r}')\bar{g}(\mathbf{r},\mathbf{r}') d\bar{\Omega}' d\bar{\Omega}, \tag{63}$$

and matrices $\mathbf{N}_c^m$ and $\mathbf{N}_m^c$ (which represent the coupling between the electric and magnetic domains) are defined by

$$N_{c_{ku}}^m = \mu_0 2\pi r_{n_{m,k}} \vec{\phi} \cdot \int_{\bar{\Omega}_c} \mathbf{w}_u^{\phi}(\mathbf{r}') g(\mathbf{r}, \mathbf{r}') d\bar{\Omega}', \tag{64}$$

where r_{n_m} is the coordinate along $\vec{r}$ of $n_{m,k}$;

$$N_{m_{ku}}^c = \varepsilon_0 \int_{e_c} \vec{e} \cdot \int_{\bar{\Omega}_m} \mathbf{w}_k^f(\mathbf{r}') \bar{g}(\mathbf{r}, \mathbf{r}') d\bar{\Omega}' d\mathbf{l}, \tag{65}$$

where $\vec{e}$ is the unit vector in the direction of e_c.

Finally, the discrete EM problem derived from (3), (31), (32), and (40) can be represented as the following algebraic system of equation

$$\begin{bmatrix} \mathbf{R}_c + i\omega \mathbf{L}_c^c & \mathbf{M}_{1/\varepsilon_0} \mathbf{C}_{\bar{\Omega}_c} \mathbf{N}_m^c \\ -\mathbf{M}_{1/\mu_0} \mathbf{G}_{\bar{\Omega}_m} \mathbf{N}_c^m & \mathbf{R}_m + i\omega \mathbf{L}_m^m + \frac{1}{i\omega} \mathbf{G}_{\bar{\Omega}_m} \mathbf{P}_m \mathbf{C}_{\bar{\Omega}_m}^a \end{bmatrix} \times \begin{bmatrix} \mathbf{j}_c \\ \mathbf{j}_m \end{bmatrix} = \begin{bmatrix} \mathbf{e}_0 \\ \mathbf{h}_0 \end{bmatrix}. \tag{66}$$

Due to the symmetry of (31) and (32), matrix blocks $(1,2)$ and $(2,1)$ should satisfy

$$\mathbf{M}_{1/\varepsilon_0} \mathbf{C}_{\bar{\Omega}_c} \mathbf{N}_m^c = -(-\mathbf{M}_{1/\mu_0} \mathbf{G}_{\bar{\Omega}_m} \mathbf{N}_c^m)^T. \tag{67}$$

However, since $\mathbf{N}_m^c$ and $\mathbf{N}_c^m$ are only *numerical approximations* of integral discrete operators, this property is numerically lost. However, (67) can be enforced resulting in a more accurate method which strongly satisfies the physical properties of the EM fields. Moreover, by substituting the matrix block $(1,2)$ with $-(2,1)^T$, matrices $\mathbf{M}_{1/\mu_0}$ and $\mathbf{N}_c^m$ are not needed anymore (or vice–versa). Thus, multiplying the second row of (66) by -1, the system can be symmetrized.

Finally, when homogeneous magnetic media are considered $\nabla \cdot \mathbf{J}_m = 0$ (i.e. $\varrho_m = 0$). This property is enforced by (66) but not in a numerically strong sense. However, the vanishing of ϱ_m can be strongly enforced by imposing

$$\mathbf{j}_m = \mathbf{G}_{\bar{\Omega}_m} \mathbf{t}_m, \tag{68}$$

where $\mathbf{t}_m$ is the array of DoFs related to a discrete vector potential associated to the nodes n_m (3–D edges n_m^{3D}) of $\mathcal{G}_{\bar{\Omega}_m}$, (except one for each magnetic sub–domain considered as reference). Then, (68) is applied to (66) and $\mathbf{G}_{\bar{\Omega}_m}$ (without one column for each magnetic sub–domain) is used to project the second matrix row of (66) into a new set of equations. The resulting system has a reduced dimension and it strongly enforces $\mathbf{C}_{\bar{\Omega}_m} \mathbf{j}_m = 0$, i.e. $\mathbf{q}_m^v = \mathbf{0}$ and $\nabla \cdot \mathbf{J}_m = 0$. Moreover, matrices $\mathbf{P}_m^{vv}$, $\mathbf{P}_m^{vs}$, and $\mathbf{P}_m^{sv}$ are not needed anymore.

IV. Comparison between the methods

The method proposed in section II is based on the amperian interpretation of the magnetization phenomena. When this approach is adopted, the inductance matrices are the only full *integral matrices* to be evaluated, resulting in a relatively easy implementation. Moreover, several analytical expressions for the self and mutual inductances of loops with rectangular cross section exist [21]. Thus, all the inductance matrices can be efficiently evaluated using analytical formulas.

The main drawback of this method consists in a poor numerical performance when magnetic media with relative high permeability are involved. Especially when they have a non–zero conductivity or when they are very close to conductive media. Indeed, the constitutive relation (4) depends on α_m that, with the increase of the relative permeability, tends to the value μ_0 (i.e. $\alpha_m \to \mu_0$ with the increasing of μ_r). For instance, from a numerical point of view, the difference between a media with $\mu_r = 1{,}000$ and $\mu_r = 10{,}000$ is left to the last significant digits of α_m and, due to *round–off* errors [22], this *numerical information* can be completely lost when floating–point arithmetic is used. When $\mathbf{F}$ is summed to other integral matrices (which are affected by numerical approximations due to the integration of the Green's function) this numerical issue is enhanced. Indeed, the numerical approximations which affect the integral matrices are orders of magnitude greater than the last significant digits of α_m. This problem is alleviated when (30) is enforced. However this is only possible when non–conductive magnetic media are considered.

The effort required by the implementation of the *coulombian* method described in section III is slightly more expensive since different integral matrices must be evaluated and matrix $\mathbf{L}_m^m$ does not allow for an easy analytical evaluation. Moreover, when properties (30) and (68) are enforced, the amperian approach leads to a magnetic matrix equation with a lower sparsity ratio ($\sim n_m^b/n_m$) while the magnetic equation of (66) remains full. However, system (66) does not suffer from the numerical issue described above for conductive magnetic media with high permeability. Moreover, when the frequency is sufficiently low, $\mathbf{L}_m^m \approx 0$. Thus, system (66) can be further simplified by neglecting the presence of the term $i\omega \mathbf{L}_m^m$ in the matrix block $(2,2)$, which leads to a relatively sparse magnetic equation when property (68) is enforced (sparsity ratio $\sim n_m^b/n_m$).

Both systems (29) and (66) are suitable for the application of low–rank approximation techniques [12], allowing a drastic reduction of the storage and the computational cost arising from the handling of full matrices. In the numerical studies, the low–rank approximation techniques described in [13] and implemented in HLIBpro library [15] has been applied to both the proposed methods. HLIBpro relies on the hierarchical ($\mathcal{H}$)-matrix representation coupled with adaptive cross approximation (ACA). Such library also provides a partitioning algorithm, based on geometric bisection, which splits the DoFs into disjoint clusters and builds a binary tree which terminates as soon as a prescribed condition is reached. However, in order to obtain matrix blocks which are actually low–rank, it is important to force the first clustering partition of the unknowns (which is viable thanks to the functionality of HLIBpro). Thus, when (29) (or (66)) is solved, $\mathbf{j}_c$ and $\mathbf{m}$ (or $\mathbf{j}_c$ and $\mathbf{j}_m$) must be subdivided into two different clusters, and $\mathbf{m}$ (or $\mathbf{j}_m$) should be further subdivided into *boundary* and *internal* unknowns. Then, as described in [13], the partitioning algorithm proceeds with the construction of the cluster tree starting from these three master cluster nodes. A completely equivalent discussion holds for $\boldsymbol{\psi}_m$ (or $\mathbf{t}_m$) when (30) (or (68)) is enforced. When these measures are embraced, thanks to the smoothness of the Green's kernel, very low compression ratios can be reached (e.g. less than 3%, as shown in the numerical studies).

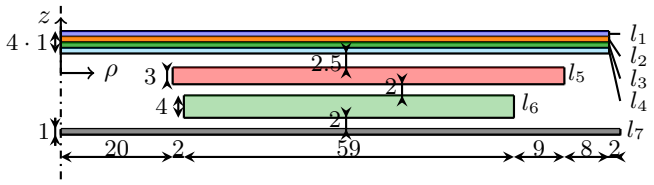

Figure 4. Axial–symmetric model of the induction cookware. Dimensions are in mm. l_1) Stainless Steel, l_2) Aluminum, l_3) Magnetic Steel, l_4) Stainless Steel, l_5) External coil, l_6) Ferrite (flux concentrator), l_7) Aluminum (shield).

Table I
MATERIAL PARAMETERS OF THE INDUCTION HEATING POT.

	l_1	l_2	l_3	l_4	l_6	l_7
σ [MS/m]	1.04	29.1	$a)0$ $b)2$	1.04	0	29.1
μ_r	1	1	$400 - i175$	1	2300	1

Finally, it is worth noting that both (29) and (66) can be adopted for the solution of steady state problems: (29) can be directly solved when $\omega = 0$ while (66) only requires a scaling of the unknowns $\mathbf{j}_m$ by $i\omega$.

Sample MATLAB® codes of the two formulation are available at https://github.com/UniPD-DII-ETCOMP/DenseMatrixMarket.

V. NUMERICAL RESULTS

Two algorithms based on the two proposed integral axisymmetric formulations have been implemented in MATLAB® and parallel MEX–FORTRAN functions based on OpenMP libraries. Moreover, the code has been also combined with HLIBpro library in a *matrix–free* logic. Thus, when HLIBpro is adopted, systems (29) and (66) are never actually assembled and stored. In the following, the code based on the formulation of section II is defined as *A–code* (Amperian code) while the one based on section III is defined as *C–code* (Coulombian code). Self inductance coefficientsare evaluated following [21], whereas mutual coefficients are numerically evaluated with 8 and 9 quadrature points. Simulations were run on a Linux machine equipped with a Xeon E5-2643 v4 processor (dual 6-core, 24 thread, @3.40 GHz) and with 512 GB of RAM.

The case of the induction cookware presented in [14] is considered. The geometry of the problem is completely described by Fig. 4. With respect of Fig. 4, layers l_1, l_2, l_3, and l_4 constitute the bottom part of the pot, layer l_5 is the external current–driven coil (the problem excitation), l_6 is the magnetic flux concentrator, and l_7 is the shield. The material parameters are the ones in Table I. With the aim of investigating the numerical behavior of the A and C–codes under different conditions, the magnetic steel (layer l_3 in Fig. 4) is modeled in two different ways: a) by non conductive magnetic media, and b) by conductive magnetic media with a conductivity of 2 MS/m. The frequency of the problem, f, is swept from 20 kHz to 100 kHz. The equivalent impedance of the device, with respect to a uniform (external) current flowing in the external coil, is modeled as $Z_{eq} = R + i\omega L$ and evaluated with the two proposed methods. Due to the strong skin effects (skin depth of $\delta \approx 0.06$ mm for the worst case), a great amount of mesh elements is required for the discretization of the conductive layers. Thus, the mesh of the induction cookware model consists of 54,120 conductive

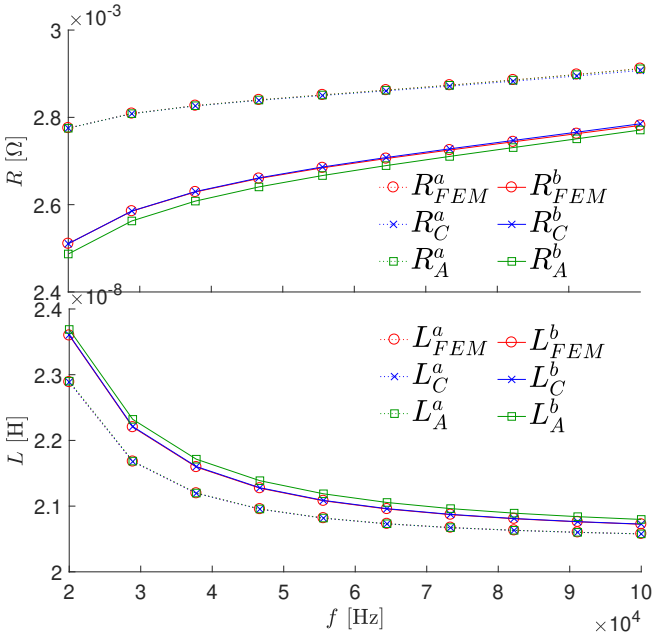

Figure 5. Z_{eq} of the induction cookware. Results obtained from A–code, C–code, and FEM for cases (a) and (b).

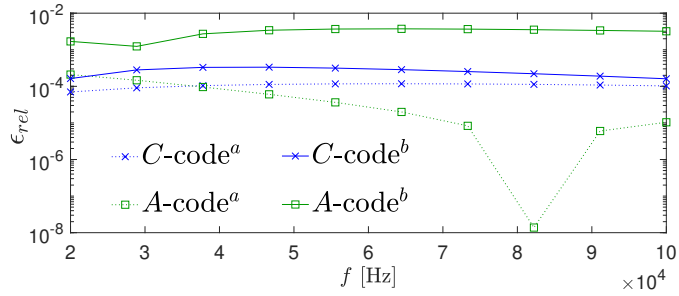

Figure 6. Relative error of $|Z_{eq}|$ for A–code and C–code for cases (a) and (b).

quadrilateral faces and 16,680 magnetic quadrilateral faces. With the aim of allowing a fair comparison, the same mesh is adopted for the A and C–codes.

In Fig. 5, the results obtained from A–code and C–code are compared with the ones from the commercial Finite Element Method (FEM) software COMSOL®, which allows for a very efficient solution of this kind of device and therefore is considered as a reference. The axisymmetric FEM model consists of 64,847 mesh elements and third order basis function.

Fig. 6 shows the relative error of the magnitude of Z_{eq} obtained from A–code and C–code with respect to FEM for both cases (a) and (b).

Results in Fig. 5 and Fig. 6 show an excellent agreement when case (a) is considered. For case (a), the simulations have been carried out with and without the imposition of (30) and (68). However, as expected, even if a little distortion on the distribution of $\mathbf{M}$ is obtained when (30) and (68) are not enforced, the results in terms of Z_{eq} differ less than 0.05%.

For case (b), C–code still shows an excellent agreement with FEM. A–code instead shows a lower accuracy, especially for the real part of Z_{eq} which is more affected by the actual

Table II
INDUCTION COOKWARE: COMPUTATIONAL DATA

	N_{DoFs}	Time [s]	PMU [GB]
FEM	1,029,074	55	4.36
A–code*	88,307	432^a+$3{,}408^s$	238
A–code$^\#$	88,307	7^a+43^s	2.8
C–code*	88,307	335^a+$3{,}308^s$	238
C–code$^\#$	88,307	7^a+44^s	3.0

*Uncompressed. $^\#$Compressed. ^{a}Assembling. ^{s}Solution.

distribution of $\mathbf{M}$, which is not enforced in a numerically strong sense. Indeed, it is worth noting that for case (b), since a conductive magnetic media is considered, (30) cannot be enforced since $\mathbf{M}$ is not curl free. Moreover, due to round–off errors, the *A*–code is very sensitive to the accuracy of the numerical integrations. However, due to the numerical nature of round–off errors, a higher accuracy in the computation of the integral matrices does not ensure to avoid this numerical issue. For the sake of comparison, the same number of Gauss points has been chosen for the *A* and *C*–codes.

In Table II the computational details of the two methods are reported for case (b) and $f = 100$ kHz. For the *A* and the *C*–codes, the computational times and the Peak Memory Usage (PMU) are reported with and without the adoption of low–rank approximation techniques. The results of Table II have been obtained *without* the imposition of (30) and (68), the compression tolerance described in [13] is set to $\varepsilon_{ACA} = 10^{-3}$ (much lower than the ones adopted in [13] for a 3–D case) and the admissibility parameter is $\eta = 2$. With this choice of ε_{ACA}, the relative error introduced by the low–rank approximation on the solution is less than 1%. Thus, it is safe to say that the errors introduced by the low–rank approximation do not noticeably affect the accuracy (results shown in Fig. 5 are the ones obtained from HLIBpro).

With respect Table II, for the uncompressed case the problem is solved with an LU decomposition of the matrix system. Instead, the compressed case is solved by means of GMRES solver with a $\mathcal{H}$–LU preconditioner. Thus, the solution time includes both the $\mathcal{H}$–LU and the GMRES solution. For both the uncompressed and compressed cases, the PMU almost coincides with the memory required for the storage of the system matrices and LU factorizations. The $\mathcal{H}$–LU is generated by imposing the same tolerance ε_{ACA} and its storage requires almost the same memory of the compressed system. As can been seen from Table II, due to the big size of the problem, the use of low–rank approximation techniques is mandatory. Indeed, the adoption of HLIBpro library allows for a drastic reduction of the computational cost required by the IE methods which become comparable with the highly optimized FEM commercial software for this kind of application.

VI. CONCLUSION

Two axisymmetric integral equations methods have been proposed. Both methods allow for conductive and magnetic media and inhomogeneous properties of the materials can be considered as well. The numerical features of the two methods have been widely discussed and compared. Most of the considerations of section IV still hold for the 3–D methods presented in [9] and [10] from which the axisymmetric methods are derived. Low–rank approximation techniques based on HLIBpro library have been successfully combined with both the proposed methods obtaining a drastic reduction of the computational cost with a truly negligible loss of accuracy. Thanks to the regularity of the axisymmetric Green's kernel, the compression ratio attained in the numerical studies is lower than the ones obtained for integral 3–D methods as in [12] and [13]. As demonstrated by the numerical results, the use of HLIBpro library widely increases the applicability of the proposed formulations that become competitive with finite element method approaches and which may become preferable when large air domains or small air gaps are considered.

REFERENCES

[1] P. Alotto et al., "A Boundary Integral Formulation on Unstructured Dual Grids for Eddy-Current Analysis in Thin Shields," *IEEE Trans. Magn.*, vol. 43, no. 4, pp. 1173-1176, April 2007.

[2] M. Spezzapria et al., "Numerical Simulation of Solid–Solid Phase Transformations During Induction Hardening Process," *IEEE Trans. Magn.*, vol. 52, no. 3, pp. 1-4, March 2016, Art no. 7402404.

[3] J. Acero et al., "Quantitative Evaluation of Induction Efficiency in Domestic Induction Heating Applications," *IEEE Trans. Magn.*, vol. 49, no. 4, pp. 1382-1389, April 2013.

[4] P. Sergeant et al., "Magnetic Shielding of Levitation Melting Devices," *IEEE Trans. Mag.*, vol. 46, no. 2, pp. 686-689, Feb. 2010.

[5] Z. Yan et al., "Numerical Prediction of Levitation Properties of HTS Bulk in High Magnetic Fields," *IEEE Trans. Appl. Supercond.*, vol. 29, no. 5, pp. 1-5, Aug. 2019, Art no. 3602805.

[6] M. Naseh and H. Heydari, "Levitation Force Maximization in HTS Magnetic Bearings Formulated by a Semianalytical Approach," *IEEE Trans. Appl. Supercond.*, vol. 27, no. 5, pp. 1-11, 2017, Art no. 5203811.

[7] J. Freidberg, *Plasma Physics and Fusion Energy*. Cambridge University Press, 2017.

[8] R. M. Fano et al., *Electromagnetic Fields, Energy, and Forces*. M.I.T. Press, 1960.

[9] R. Torchio et al., "A 3-D PEEC Formulation Based on the Cell Method for Full-Wave Analyses With Conductive, Dielectric, and Magnetic Media," *IEEE Trans. Magn.*, vol. 54, no. 3, pp. 1-4, 2018.

[10] R. Torchio et al., "An Extension of Unstructured-PEEC Method to Magnetic Media," *IEEE Trans. Magn.*, vol. 55, no. 6, pp. 1-4, 2019.

[11] R. Torchio, "A Volume PEEC Formulation Based on the Cell Method for Electromagnetic Problems from Low to High Frequency," *IEEE Trans. Antennas Propag.*. doi: 10.1109/TAP.2019.2927789

[12] R. Torchio et al., "PEEC-Based Analysis of Complex Fusion Magnets During Fast Voltage Transients With H-Matrix Compression," *IEEE Trans. Magn.*, vol. 53, no. 6, pp. 1-4, 2017.

[13] D. Voltolina et al., "High-Performance PEEC Analysis of Electromagnetic Scatterers," *IEEE Trans. Magn.*, vol. 55, no. 6, pp. 1-4, 2019.

[14] F. Moro et al., "Impedance design of cooking appliances with multilayer induction-efficient cookware," *IECON 2013 - 39th Annual Conference of the IEEE Industrial Electronics Society*, Vienna, 2013, pp. 5040-5045.

[15] R. Kriemann. HLIBPro (v.2.7.1). Accessed: May 18, 2019. [Online]. Available: http://www.hlibpro.com

[16] W. Alexander, "Generalized axially symmetric potential theory", *Bulletin of the American Mathematical Society*, vol. 59, no. 1, pp. 20–38, 1953.

[17] O. Ciftja and I. Hysi, "The electrostatic potential of a uniformly charged disk as the source of novel mathematical identities", *Applied Mathematics Letters*, vol. 24, no. 11, pp. 1919 - 1923, 2011.

[18] J.-M. Huré, "Solutions of the axi-symmetric Poisson equation from elliptic integrals", *Astronomy and Astrophysics*, 2004.

[19] J. Simpson et al., "Simple Analytic Expressions for the Magnetic Field of a Circular Current Loop", *NASA Technical Documents*, 2003.

[20] S. Datta, "Electric and Magnetic Fields from a Circular Coil Using Elliptic Integrals", *Phys. Educ.*, 2007.

[21] G. Chitarin et al., "An integral formulation for eddy current analyses in axisymmetric configurations," *IEEE Trans Magn.*, vol. 25, no. 5, pp. 4330-4342, Sept. 1989.

[22] A. M. Turing, "Rounding-Off Errors in Matrix Process", *Q. J. Mech. Appl. Math.*. vol. 1, no. 287, 1948.